Effects of elastic anisotropy on strain distributions in decahedral gold nanoparticles

CRAIG L. JOHNSON[1]*, ETIENNE SNOECK[1], MANEX EZCURDIA[1], BENITO RODRÍGUEZ-GONZÁLEZ[2], ISABEL PASTORIZA-SANTOS[2], LUIS M. LIZ-MARZÁN[2] AND MARTIN J. HŸTCH[1]

[1]CEMES-CNRS, 29, rue Jeanne-Marvig 31055 Toulouse, France
[2]Departamento de Químíca Física and Unidad Asociada CSIC, Universidade de Vigo, 36310 Vigo, Spain
*e-mail: johnson@cemes.fr

Metallic nanoparticles exhibit exceptional optoelectronic properties with applications in plasmonics, biosensing and nanomedicine[1–5]. Recently, new synthesis techniques have enabled precise control over the sizes and shapes of metal nanoparticles[6–8], occasionally leading to morphologies that cannot be properly characterized using standard techniques. An example is five-fold-twinned decahedral Au nanoparticles, which are intrinsically strained as a result of their unique geometry. Various competing models have been proposed to predict the strain states of such nanoparticles. Here, we present a detailed analysis of the internal structure of a decahedral Au nanoparticle using aberration-corrected high-resolution electron microscopy and strain mapping. Our measurements confirm the presence of a disclination, which is consistent with the commonly accepted strain model. However, we also observed shear gradients, which are absent from the models. By comparing our local strain determinations with finite-element calculations, we show the effect of elastic anisotropy on the strain state in these nanoparticles.

Recently, a resurgence of interest in metal nanoparticles has resulted from their potential applications in the emerging field of plasmonics[1,2]. Plasmonics uses the unique optical properties of metallic nanomaterials to manipulate the transfer of light on the nanoscale and is a promising technology for integrating the large data-carrying capacity of optical interconnects with nanoscale electronic devices. Plasmonic metal nanoparticles also show potential for biosensing[3,4] and cancer therapy[5]. The optical response of these metal nanoparticles is both size and shape dependent and locally variable[6]. This sensitivity to morphology makes precise control over the growth of these nanoparticles and knowledge of their external and internal structures essential.

Sánchez-Iglesias and co-workers recently reported a method for synthesizing uniformly sized decahedral Au nanoparticles that exhibit striking optical properties[7,8]. The prominent structural feature of decahedral particles is the non-crystallographic five-fold rotational symmetry about the [110] axis, which coincides with the line of intersection of five twin boundaries. This structure occurs in nanoparticles of all of the face-centred-cubic (f.c.c.) metals, many of their alloys, and other materials including Si and Ge. Furthermore, five-fold twinning also occurs in many differently composed nanowires and nanorods[9]. Accordingly, decahedral particles and five-fold twinning have been studied extensively through both experiment and theory[10–13].

In the simple solid-geometry model (Fig. 1), the decahedral particles are composed of five tetrahedral subunits with the f.c.c. crystal structure and {111} crystallographic faces. In addition to sharing the one edge coinciding with the five-fold axis, the subunits are joined to adjacent tetrahedra by twin boundaries. However, the tetrahedra, packed in this manner, do not completely fill space (Fig. 1b) and a solid-angle deficiency remains. As a result of this deficiency, the decahedral particles must be strained and/or contain defects. In the smallest Au particles (<10 nm), the decahedral structure occurs but is unstable, and, in much larger particles, dislocations and stacking faults commonly occur. Intermediate-sized particles, however, have stable decahedral structures that are free of extended defects.

Two competing models for the internal structure of the defect-free decahedral particles have been debated. First, Bagley proposed that the solid-angle deficiency could be accommodated by a homogeneous strain, that is, a structural transformation from f.c.c. to an orthorhombic crystal structure[14,15]. On the other hand, early electron microscope studies showed evidence for inhomogeneous strain distributions[16–19], and a disclination model was proposed[20]. In the disclination model, a single wedge disclination coinciding with the five-fold axis removes the solid-angle deficiency, produces an inhomogeneous strain field and significantly reduces the strain-energy density within the particles relative to the homogeneous-strain models[12,21]. Both the homogeneous- and inhomogeneous-strain models have been alternatively invoked to explain the results of electron microscopy experiments on decahedral particles. The history of this debate is outlined in reviews by Gryaznov et al. and Hofmeister[12,22]. Eventually, on the basis of detailed experiments and analyses, Marks convincingly argued in favour of the inhomogeneous-strain model[13]. However, although experimental work showed conclusively that the strains were inhomogeneous, quantitative strain measurements were not obtained and the adoption of the disclination model depended largely on arguments from elastic theory[13,21]. More recently, observations of In and Pb decahedral particles suggest a possible third model in which
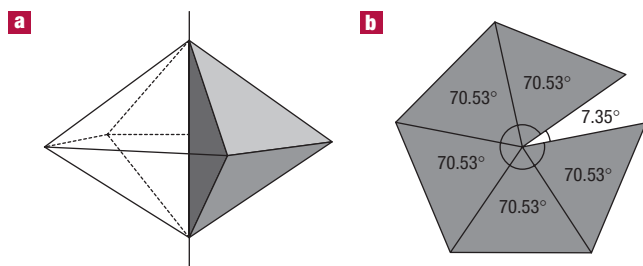
Figure 1 Decahedral geometry of Au nanoparticles. a, The shaded part of the diagram highlights one of five tetrahedral subunits that constitute the decahedral particle. The subunits have {111} crystal faces and are arranged about the five-fold-rotation axis parallel to [110] (marked by the vertical line). The light grey triangles represent the top and bottom {111} planes of the decahedron, and the dark grey triangle represents one of the internal twin interfaces that join adjacent tetrahedra. **b,** For perfect f.c.c. tetrahedral subunits, the angle between adjacent {111} faces, illustrated here in the [110] projection, is 70.53°, which results in a 7.35° solid-angle deficiency. As a result of this deficiency, real nanoparticles must contain defects or be intrinsically strained.

some tetrahedral segments are transformed homogeneously to a body-centred tetragonal structure, whereas adjacent segments in the same particle remain f.c.c. (refs 23,24).

Using aberration-corrected high-resolution electron microscopy (HREM) and geometric phase analysis[25], we have quantitatively determined the local plane strain (strain in the plane orthogonal to the five-fold axis) in a decahedral particle with a radius of 17 nm. The application of aberration correction for imaging decahedral particles has important advantages: (1) minimized delocalization of the image contrast at interfaces, which results in perfectly imaged twin boundaries; and (2) enhanced image contrast, which results in improved spatial resolution of the final strain maps. Our observations indicate that the nanoparticles do indeed contain disclinations; however, the strain distributions deviate significantly from those predicted by the commonly accepted elastic models.

The aberration-free HREM image (Fig. 2a) reveals that the nanoparticle is roughly pentagonal in the [110] projection and composed of five domains. Each domain is approximately the same size, and the core of the particle (the position of the five-fold axis where the twin planes intersect) occurs at its geometric centre. The five-fold symmetry is readily apparent in the diffractogram (Fig. 2a, inset). The twin boundaries and the interiors of the domains are free of defects. The particle is rounded compared with an ideal pentagonal projection in the proximity of the twin planes, and in some cases, small re-entrant facets occur at the boundaries. The deviation from ideal decahedral geometry is difficult to quantify from HREM images alone; however, previous microscopic analyses of these samples[7,8] and electron-holographic analyses indicate that the {111} faceting and the nominal decahedral geometry is preserved. The absence of contrast reversals in the image through the thickness of the particle and the absence of delocalized contrast at the twin boundaries is revealed in the enlarged images of the core (Fig. 2b) and the edge of the particle (Fig. 2c). This uniformity of contrast, an advantage of aberration-corrected imaging, minimizes the possibility of image artefacts that might confuse the interpretation of the strain measurements.

By analysing the HREM image with geometric phase analysis, we measured the internal rigid-body rotation of the lattice and the intrinsic strains in the particle. The deformations in each segment were determined piecewise and are relative to an internal reference

lattice. The piecewise analysis enabled us to uniquely determine the strain gradients within the segments, but limits our ability to address sharp changes at the boundaries between the segments. The reference lattice is a selected region at the centre of each segment. We use the centres of the segments because they coincide with the planes of mirror symmetry both in the tetrahedral geometry and the crystal structure. However, the strain and rotation gradients are independent of the reference position. Indeed, a shift of the reference area results only in the addition of a constant value to the strain and rotation fields.

The rotation of the lattice around the particle core is primarily accomplished by the 70.53° twin rotation. In total, the twinning rotates the lattice by 352.65°. This twin rotation at the boundaries is excluded from our rigid-body rotation measurement (Fig. 3a), because the reference for each segment is internal. The rigid-body rotations in Fig. 3a are smoothly changing, internal to the segments and independent of radius. To quantify the disclination power (magnitude of the rotational distortion), we fit tangential profiles of the internal anticlockwise rotations in each segment with linear regressions. The disclination power in a single segment is determined from the difference between the minimum and maximum of the linear fit at the angular position of the interfaces bounding the segment. The individual rotations for segments 1 to 5 (see Fig. 3b) are 0.76°, 1.11°, 0.44°, 1.19° and 0.81°, respectively, and the average per segment is 0.86°. The sum of these individual measurements gives the total disclination power of $+4.3 \pm 0.1°$. Although this value falls short of the 7.35° required by the decahedral geometry, the lattice rotation in the segments uniquely reveals the presence of a disclination-like rotational distortion. However, the shortfall of the rigid-body rotation with respect to the solid-angle deficiency indicates that some other form of distortion must be present or that the elastic response of the particle cannot be modelled as a simple cylinder with homogeneous elastic properties.

We carried out a series of finite-element calculations to analyse the effects of morphology and elastic anisotropy on the rotation and strain fields of the decahedral particles. The effects of elastic anisotropy were evaluated by comparing isotropic and anisotropic models. The anisotropic calculations accounted for variations in the elastic response of gold in different crystallographic directions. Shape was analysed by comparing cylindrical models with pentagonal prismatic and full three-dimensional models.

In the isotropic calculations, the rigid-body rotations are purely internal and continuous regardless of the model geometry. Furthermore, the isotropic rotations have nearly the same linear slope and, therefore, the same total rotation of $\sim7.5°$ (the cylindrical model is shown in Fig. 3b). On the other hand, the rotations determined from the anisotropic calculations have reduced internal rotations and discontinuities in the rotation at the interfaces between the segments. The step height, that is, the magnitude of the discontinuities at the interfaces, seems to be inversely proportional to the internal rotations in the segments. As a result, the total rotations (internal rotation + steps at the interfaces) for the anisotropic models are all about 5.7°. The fit to the rotation in our Au nanoparticle was directly compared with the isotropic rotations and the internal rotations from the anisotropic calculations. The measured internal rotation fits perfectly within the range of the rotations calculated using the anisotropic models. Indeed, the measured rotation fits almost exactly with the cylindrical anisotropic model, which has a rotation step of 0.24° at each interface and 0.90° internal rotation in each segment (total internal rotation = 4.5°). On the basis of the comparison to the finite-element models, we can propose a possible rotation step of $\sim0.25°$ for the Au decahedral particle.

Therefore, elastic anisotropy explains the reduced rotation that occurs in the particle. The discontinuities at the interface, which
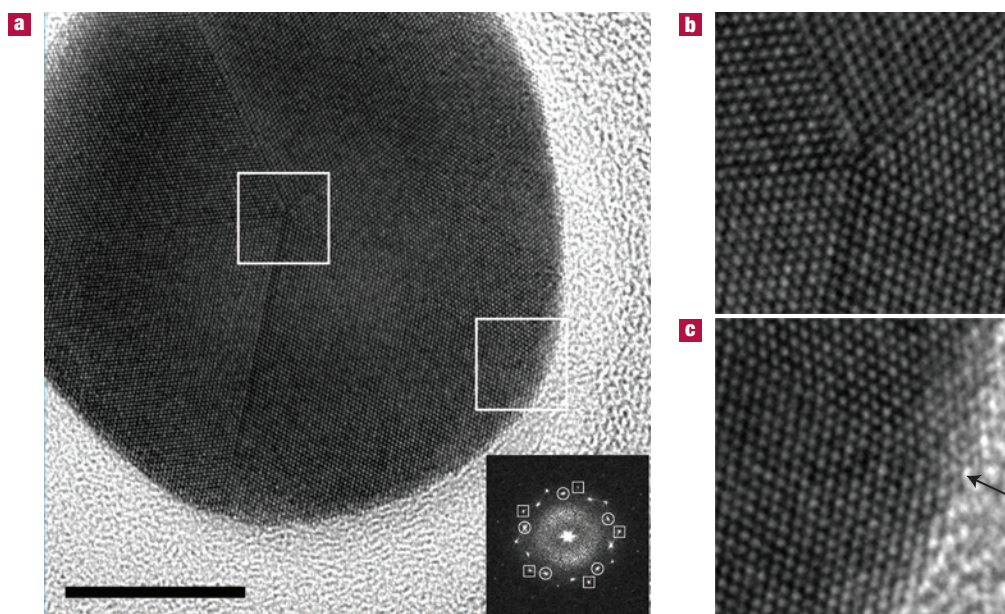
Figure 2 Aberration-corrected HREM image of a 17-nm-radius defect-free decahedral Au nanoparticle. a, The image shows the five-fold rotational symmetry marked by twin boundaries that originate at the centre of the particle. Equivalent 111 and 002 reflections in the diffractogram (inset) are marked by circles and squares, respectively. The scale bar is 10 nm. **b**, An expanded view of the particle core (marked by the square at the centre of **a**) shows the intersection of the five twin boundaries. **c**, An enlarged view of the particle edge (region marked by a square on the right side of **a**) shows the termination of one of the twin interfaces.

are not directly observable in our experimental measurements, may provide further rotation. However, interestingly, the total rotations predicted by the finite-element models, even including the boundary steps, are still less than the 7.35° necessary to fill the solid-angle deficiency. Therefore, a further distortion mechanism is required to satisfy the constraints of the decahedral geometry.

Isotropic elastic theory for disclinations predicts shear strain ($\varepsilon_{r\theta}$) to be zero everywhere in the particle. Indeed, $\varepsilon_{r\theta}$ must be zero in the isotropic case, because a shear implies a change of the angle between the {111} planes. However, our experimental measurement (Fig. 4) reveals a gradient in $\varepsilon_{r\theta}$ from one boundary to the next. The average maximum and minimum of linear fits to the shear gradients (Fig. 4b) gives the average shear at the interfaces ($\langle\varepsilon_{r\theta}\rangle = \pm 0.54\%$). By the small-angle approximation, $\langle\varepsilon_{r\theta}\rangle$ is equal to the change in the {111} angle in radians, which, in this case, means an increase in the {111} angle of 0.6° for each subunit and 3° for the entire particle. The anisotropic finite-element models also contain shear gradients, whereas the isotropic models have no shear component. Most importantly, the total angle increase resulting from the shear fully accounts for the residual solid-angle deficiency that was not filled by the internal lattice rotation. The 0.54% shear strain at the boundaries combined with the 4.3° disclination-like lattice rotation fully explains how the internal structure of the decahedral particle accommodates the geometric constraints of the solid-angle deficiency. However, two differences between our measurements and the finite-element calculations require some discussion.

First, discontinuities occur in the simulated rotation fields at the twin boundaries. This result seems inconsistent with the measured rotation field. However, our measurements are limited to the relative distortions within each segment, and, discontinuities directly coinciding with the interfaces, if they occur, would be excluded. Furthermore, we have focused, so far, on the average results of linear fits to the rotation. Close examination of the

rotation profiles in the individual segments shows that they deviate from the average slope and deviate from linearity close to the twin boundaries. The deviation of the measured slopes in some segments (for example, the internal rotation in segment 3 (see Fig. 3b) is only 0.44°, which is nearly half of the average value of 0.86°) may provide indirect evidence that discontinuities in the rotation do occur at some of the boundaries of our Au decahedral particle.

Second, we determined the shears at the twin boundaries from linear fits to the measurements. In comparison, the tangential profile of the shear strain from the finite-element calculations rises to a maximum and then decreases slightly just before the interface (Fig. 4b). The shear at the interface is less than half that of the shears measured from the linear fits. Therefore, the linear fits may represent an upper bound for the shears there. If discontinuities occur at the boundaries, as is suggested by the finite-element calculations, then the shears at the boundaries may be less than those reported above.
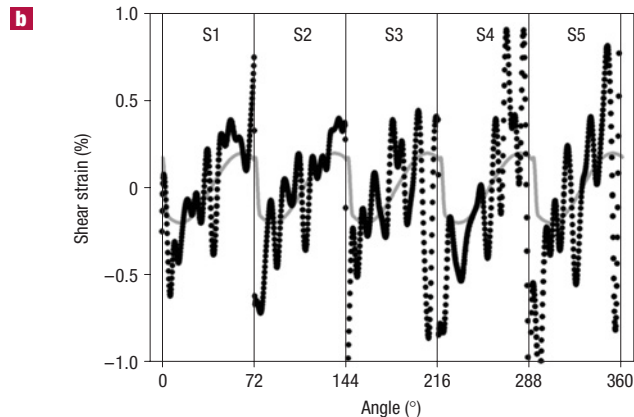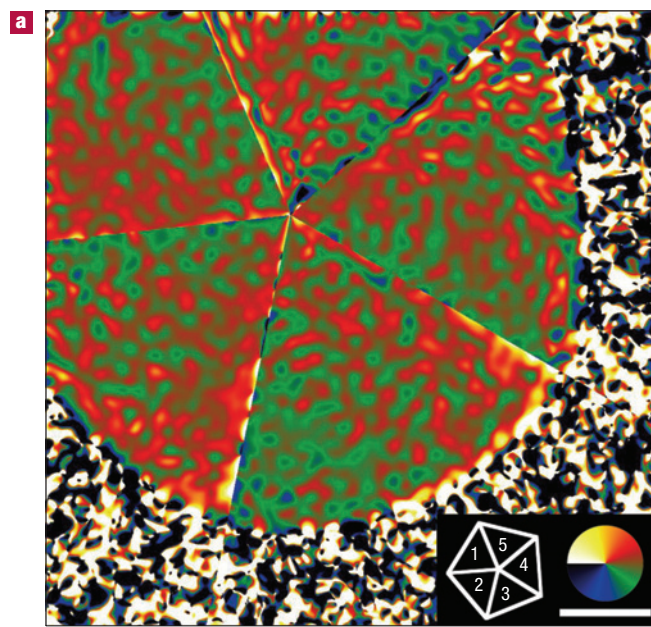
Despite these uncertainties, our measurements indicate that an internal lattice rotation of 4.3° coupled with small shear strains of as much as 0.54% accommodate the 7.3° solid-angle deficiency in the decahedral Au nanoparticle we studied. Comparison of the experimental results with finite-element calculations indicates that this partitioning of the distortion between the lattice rotation and the shear results from the elastic anisotropy of Au. This effect of anisotropy can be explained by the elastic compatibility conditions[26]. The compatibility conditions require that displacements and strain parallel to coherent interfaces, such as twin boundaries, be continuous despite the orientational inhomogeneity. For example, if a twinned anisotropic material is subjected to an external stress, each side of the boundary has a different orientation and, therefore, a different elastic response. The compatibility stresses are generated to compensate these different responses and ensure that the strains and displacements in the direction parallel to the boundary are continuous. These
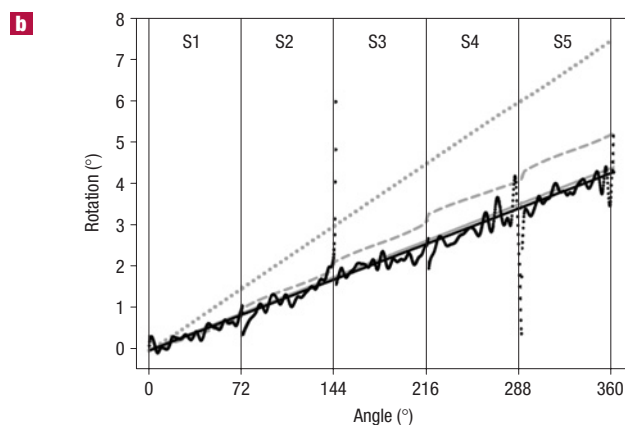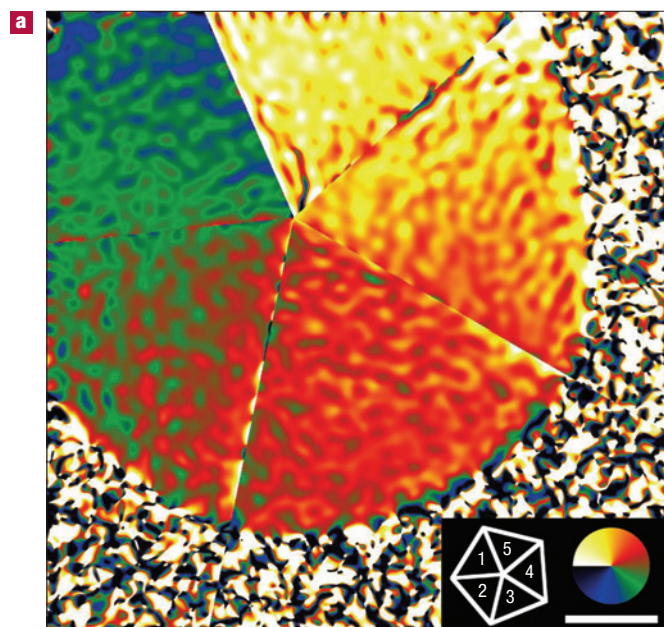
Figure 3 Lattice-rotation distribution in the decahedral Au nanoparticle in Fig. 2a. **a**, The rotation map gives the internal rigid-body rotation of the crystallographic lattice. The scale bar is 5 nm and the colour scale indicates -2 to $+5°$ rotation. **b**, By comparing the tangential profiles of the experimental internal rotation (experimental data: black circles; linear fit: black line) and the finite-element models (isotropic cylinder: grey dotted line; anisotropic cylinder: grey dashed line; anisotropic cylinder, internal rotation only: grey solid line), we determined that elastic anisotropy results in a decreased internal lattice rotation of only $4.3°$ for the nanoparticle compared with $7.35°$ expected from the geometric constraints and predicted by isotropic elastic theory. The numbering S1 to S5 refers to the schematic diagram in the inset in **a**.

Figure 4 Shear-strain distribution in the decahedral Au nanoparticle in Fig. 2a. **a**, The shear-strain map shows the shear gradient across each segment of the decahedral particle. The scale bar is 5 nm and the colour scale indicates -5 to $+5\%$ shear strain. **b**, From the tangential profiles of the measured shear (experimental data: black circles) and the shear determined from the finite-element calculations (anisotropic cylinder: grey solid line), we determined minimum and maximum shears at the boundaries of each subunit to be $\pm0.54\%$, which translates to a $0.6°$ increase in the angle between {111} planes. In total, this increase fills the residual solid-angle deficiency not filled by the rotational distortion. The numbering S1 to S5 refers to the schematic diagram in the inset in **a**.

compatibility stresses are important for interfaces in strained anisotropic materials such as our Au decahedral particle. A full analysis of the elastic compatibility for the decahedral particles is beyond the scope of this letter. However, the discontinuities that occur in the finite-element calculations are probably a consequence of compatibility stresses because they do not occur in the isotropic models. Our results do not exclude the possibility of boundary discontinuities and, indeed, may provide indirect evidence of their presence.

Our results show that elastic anisotropy is critical for understanding the strain distributions and the internal structures in decahedral nanoparticles. We expect new insights regarding the properties of multiply twinned nanoparticles to come from continued quantitative investigation of their internal structures through the combination of advanced electron microscopy and computer simulations. The effects of morphological details, such as sharp pentagonal corners and faceting, on the local atomic structure are intriguing prospects for study. The internal structure of these complex decahedral particles will determine their growth and stability as well as affect their surface structures and, therefore, will be of great importance for engineering their electronic and optical properties.

METHODS

HREM images were obtained using the spherical-aberration-corrected transmission electron microscope in Toulouse, a Tecnai F20 ST (FEI) microscope fitted with an imaging aberration corrector (CEOS), a rotatable electron biprism (FEI), a 2 k CCD (charge-coupled device) camera (Gatan) and an imaging filter (Gatan Tridiem). Image analysis was done using GPA Phase[27] and DigitalMicrograph (Gatan) software. Microscope distortions were calibrated to obtain highly accurate (<0.1% strain), high-spatial-resolution (<1 nm) maps of the individual components of the strain and rotation tensor in the decahedral particle[28].

Pure Au nanoparticles of various sizes were grown following the synthesis procedures described by Sánchez-Iglesias *et al.*[8]. The synthesis yields primarily decahedral nanoparticles with precisely controlled size ranges and minor amounts of particles with other morphologies.

Finite-element calculations were done using COMSOL Multiphysics software[29]. Finite-element analysis is a versatile computer simulation technique used for continuum modelling of deformation in materials[30]. The simulations account for many materials properties including elastic anisotropy, thermal expansion and three-dimensional object shape. We generated cylinder, pentagonal prism and decahedron models. Each model is composed of five segments. Initially, four of the segments are bounded on either side with {111} crystal faces separated by an angle of 70.53° in each segment. The tetrahedral angle in the fifth segment is larger (initially $70.53 + 7.35°$). This fifth segment is artificially contracted by specifying a thermal-expansion coefficient such that a decrease in the temperature of the system by 1° will reduce the tetrahedral angle for the segment to 72°. The other segments are unaffected by the temperature change. After the relaxation, however, all of the segments are strained and have tetrahedral angles of 72°. To prevent rigid-body motion of the model out of the known coordinate system, we fixed the interfacial plane opposite the artificially contracted segment. As a result of these configurations, the fifth segment contains no usable information, and, for our comparisons with the experimental data, we used the average data from the segments on either side of the fixed plane. For the cylinder and prism models, the top and bottom planes were also fixed.

References

1. Barnes, W. L., Dereux, A. & Ebbesen, T. W. Surface plasmon subwavelength optics. *Nature* **424**, 824–830 (2003).
2. Zia, R., Schuller, J. A., Chandran, A. & Brongersma, M. L. Plasmonics: The next chip-scale technology. *Mater. Today* **9**, 20–27 (2006).
3. Willets, K. A. & Van Duyne, R. P. Localized surface plasmon resonance spectroscopy and sensing. *Annu. Rev. Phys. Chem.* **58**, 267–297 (2007).
4. Zhao, J., Zhang, X. Y., Yonzon, C. R., Haes, A. J. & Van Duyne, R. P. Localized surface plasmon resonance biosensors. *Nanomedicine* **1**, 219–228 (2006).
5. Jain, P. K., El-Sayed, I. H. & El-Sayed, M. A. Au nanoparticles target cancer. *Nano Today* **2**, 18–29 (2007).
6. Nelayah, J. *et al.* Mapping surface plasmons on a single metallic nanoparticle. *Nature Phys.* **3**, 348–353 (2007).
7. Pastoriza-Santos, I., Sánchez-Iglesias, A., García de Abajo, F. J. & Liz-Marzán, L. M. Environmental optical sensitivity of gold nanodecahedra. *Adv. Funct. Mater.* **17**, 1443–1450 (2007).
8. Sánchez-Iglesias, A. *et al.* Synthesis and optical properties of gold nanodecahedra with size control. *Adv. Mater.* **18**, 2529–2534 (2006).
9. Reyes-Gasga, J. *et al.* On the structure of nanorods and nanowires with pentagonal cross-sections. *J. Cryst. Growth* **286**, 162–172 (2006).
10. Kirkland, A. I., Edwards, P. P., Jefferson, D. A. & Duff, D. G. The structure, characterization, and evolution of colloidal metals. *Annu. Rep. Prog. Chem. C* **87**, 247–304 (1990).
11. Yacamán, M. J. & Avalos-Borja, M. Electron-microscopy of metallic nanoparticles using high-resolution and medium-resolution techniques. *Catal. Rev.-Sci. Eng.* **34**, 55–127 (1992).
12. Gryaznov, V. G. *et al.* Pentagonal symmetry and disclinations in small particles. *Cryst. Res. Technol.* **34**, 1091–1119 (1999).
13. Marks, L. D. Inhomogeneous strains in small particles. *Surf. Sci.* **150**, 302–318 (1985).
14. Bagley, B. G. A dense packing of hard spheres with five-fold symmetry. *Nature* **208**, 674–675 (1965).
15. Yang, C. Y. Crystallography of decahedral and icosahedral particles.1. Geometry of twinning. *J. Cryst. Growth* **47**, 274–282 (1979).
16. Allpress, J. G. & Sanders, J. V. The structure and orientation of crystals in deposits of metals on micas. *Surf. Sci.* **7**, 1–25 (1967).
17. Ino, S. Epitaxial growth of metals on rocksalt faces cleaved in vacuum. II. Orientation and structure of gold particles formed in ultrahigh vacuum. *J. Phys. Soc. Japan* **21**, 346–362 (1966).
18. Ino, S. & Ogawa, T. Multiply twinned particles at earlier stages of gold film formation on alkalihalide crystals. *J. Phys. Soc. Japan* **22**, 1365–1374 (1969).
19. Marks, L. D. & Howie, A. Multiply-twinned particles in silver catalysts. *Nature* **282**, 196–198 (1979).
20. deWit, R. Partial disclinations. *J. Phys. C* **5**, 529–534 (1972).
21. Howie, A. & Marks, L. D. Elastic strains and the energy balance for multiply twinned particles. *Phil. Mag. A* **49**, 95–109 (1984).
22. Hofmeister, H. Forty-years study of five-fold twinned structures in small particles and thin films. *Cryst. Res. Technol.* **33**, 3–25 (1998).
23. Chen, Q., Tanaka, M. & Furuya, K. Unusual crystallographic structure and its fluctuation of indium nanoparticles as-deposited and observed with HRTEM using the UHV-DC-TEM system. *Surf. Sci.* **440**, 398–406 (1999).
24. Wu, Y., Chen, Q., Takeguchi, M. & Furuya, K. High-resolution transmission electron microscopy study on the anomalous structure of lead nanoparticles with UHV-MBE-TEM system. *Surf. Sci.* **462**, 203–210 (2000).
25. Hÿtch, M. J., Snoeck, E. & Kilaas, R. Quantitative measurement of displacement and strain fields from HREM micrographs. *Ultramicroscopy* **74**, 131–146 (1998).
26. Sutton, A. P. & Balluffi, R. W. in *Interfaces in Crystalline Materials* (ed. Brook, R. J. *et al.*) (Clarendon, Oxford, 1995).
27. <http://www.hremresearch.com>.
28. Hüe, F. *et al.* Calibration of projector lens distortions. *J. Electron Microsc.* **54**, 181–190 (2005).
29. <http://www.comsol.fr>.
30. Huebner, K. H. H., Dewhirst, D. L., Smith, D. E. & Byrom, T. G. *The Finite Element Method for Engineers* (Wiley, New York, 2001).

Author contributions

C.L.J., E.S., M.E. and M.J.H. carried out imaging, analysis and modelling. B.R.-G., I.P.-S. and L.M.L.-M. carried out particle synthesis.

5